nature communications

Article

https://doi.org/10.1038/s41467-024-54325-8

Ultra-fast photoelectron transfer in bimetallic porphyrin optoelectrode for single neuron modulation

Received: 18 May 2024

Accepted: 6 November 2024

Jian Chen[1,7], Feixiang Chen[1,7], Xueli Wang[2,7], Hongjun Zhuang[3], Mengnan Guo[1], Luo Wang[1], Junze Xie[1], Le Zhang[4], Hao Liu[1], Yuhan Shi[5], Jiajia Zhou[4], Xinjie Mao[1], Muyao Lv[1], Xingwu Jiang[1], Jinquan Chen[2] ✉, Yanyan Liu[1] ✉, Dayong Jin[4,6] ✉ & Wenbo Bu[1] ✉

Shrinking the size of photoelectrodes into the nanoscale will enable the precise modulation of cellular and subcellular behaviors of a single neuron and neural circuits. However, compared to photovoltaic devices, the reduced size causes the compromised efficiencies. Here, we present a highly efficient nanoelectrode based on bimetallic zinc and gold porphyrin (ZnAuPN). Upon light excitation, we observe ultrafast energy transfer (~66 ps) and charge transfer (~0.5 ps) through the porphyrin ring, enabling 97% efficiency in separating and transferring photoinduced charges to single Au-atom centers. Leveraging these isolated Au atoms as stimulating electrode arrays, we achieve significant photocurrent injection in single neurons, triggering action potential with millisecond light pulses. Notably, Extracranial near-infrared light irradiation of the motor cortex induces neuronal firing and enhances mouse movement. These results show the potential of nanoscale optoelectrodes for high spatiotemporal modulation of neuronal networks without the need for gene transfection in optogenetics.

Timingly modulation of single neurons with high temporal and spatial precision will open up new frontiers to treat the neuron degenerative diseases, as well as studying neurons' computations and outputs according to the different timing and context of input signals. Optogenetics, as a typical light-control method, can enable the temporally precise control of specific cell types, but the needs for genetic modification and high-intensity of laser irradiation limit its translational potentials[1,2]. Photoelectric (PE) devices have been extensively developed by converting the incident photons into the ionic current for electrical nerve stimulation[3–6], but their large footprint, at the device/neuron interface, causes an inefficient electric charge injection in the neuron as referred to the Gouy–Chapman theory[7], which induces an inaccurate and ineffective regulation of nerve actions[8,9]. Substantially shrinking the dimensions of PE devices towards the size of a single neuron is desirable but often at expense of the photoelectrical properties[10,11].

Large aromatic molecules with an extended π-electron system can absorb visible light to form organic PE devices[12]. Porphyrins, as the core part of chlorophyll, become an excellent choice due to their robust abilities in light harvesting and fast energy conversion[13]. Specifically, metal derivatives of porphyrins have been widely used to construct supramolecular donor-acceptor systems, since the p and

---

[1]Department of Materials Science and State Key Laboratory of Molecular Engineering of Polymers, Academy for Engineering and Technology, Fudan University, Shanghai, China. [2]State Key Laboratory of Precision Spectroscopy, East China Normal University, Shanghai, China. [3]Research Center for Translational Medicine, The First Affiliated Hospital of Xiamen University, School of Medicine, Xiamen University, Xiamen, China. [4]Institute for Biomedical Materials and Devices (IBMD), Faculty of Science, University of Technology Sydney, Sydney, NSW, Australia. [5]Baylor College of medicine, Houston, TX, USA. [6]Eastern Institute for Advanced Study, Eastern Institute of Technology, Ningbo, Zhejiang, China. [7]These authors contributed equally: Jian Chen, Feixiang Chen, Xueli Wang. ✉e-mail: jqchen@lps.ecnu.edu.cn; liuyyan@fudan.edu.cn; dayong.Jin@uts.edu.au; wbbu@fudan.edu.cn

n-type conduction can be modulated by the presence of transition *d*-metals (Zn^{2+}, Fe^{2+}, Cu^{2+}, Co^{2+}, Ni^{2+}, etc.) coordination in the aromatics[14,15]. The geometrical features of the donor-acceptor porphyrins and their relations to the mechanisms of photoinduced charge transfer and electronic excitation energy transfer are yet to be characterized and understood. Encouragingly, a bisporphyrin Bionics design, comprising zinc(II) porphyrin (electron donor) and gold(III) porphyrin (electron acceptor) that holds in an oblique orientation, can undergo intramolecular electron transfer with almost unit quantum efficiency under the visible light excitation[16].

We anticipate that the rationale design, synthesis, characterization and application of a bisporphyrin nano-system will enable the robust charge injection in neurons for precise modulation. As a result, the bimetallic zinc and gold porphyrins 2D nanosheets (ZnAuPN) were constructed via the metal-ligand axial coordination approach[17], allowing a highly efficient photoinduced charge separation and electric charge injection into single neuron (Fig. 1A). Due to the reduced HOMO–LUMO gap as the result of the pi-cloud extension along the porphyrin ring by the metal-ligand interactions, the ultrafast intermolecular energy transfer process (~66 ps) from zinc porphyrin (ZnP) to the adjacent gold porphyrin (AuP^+) was observed. Due to the heavy atom effect of Au, the excited electron can be transferred over AuP^+ to its Au-atom center at ultrafast relaxation of only 0.5 ps, thereby forming the array of electron-rich single-Au electrodes for the robust charge injection at the ZnAuPN/neuron interface (Fig. 1B). When the Zn/Au ratio reaches ~1:1, it produces a substantial photocurrent of up to ~10.0 nA at 59.24 mW/cm² under a 670 nm laser pulse of 10 ms, which is significantly higher than the ~0.12 nA current generated by a silicon nanowire electrode[3]. For single neuron, the injected charge was estimated to be ~4 pC within 1 ms when irradiated with a 670 nm laser, which is sufficient to elicit an action potential given the excitation threshold is around 3 pC[18]. This enables the modulation of single neuron with millisecond resolution. Moreover, when ZnP is partly substituted by AuP^+, the two-photon absorption cross section was found doubled to 4369 GM (Göppert–Mayer)[19], favorable for deep brain modulations. This enhancement opens up possibilities for more targeted and effective manipulation of neural activity within deeper brain regions.

Results

Synthesis and characterization of ZnAuPN

The host nanomaterials of monometallic zinc porphyrin self-assembled nanosheets (ZnPN) were prepared via the acid-base neutralization reaction[20]. The bimetallic ZnAuPN was formed by partially substituting Zn with Au[21], characterized by the transmission electron microscope (TEM) measurement (Fig. 1C and Fig. S1a). The final nanodevice was measured as 150 nm long, 80 nm wide (Fig. S1b, c), and 35 nm thick (Fig. 1D) by scanning electron microscope (SEM) and

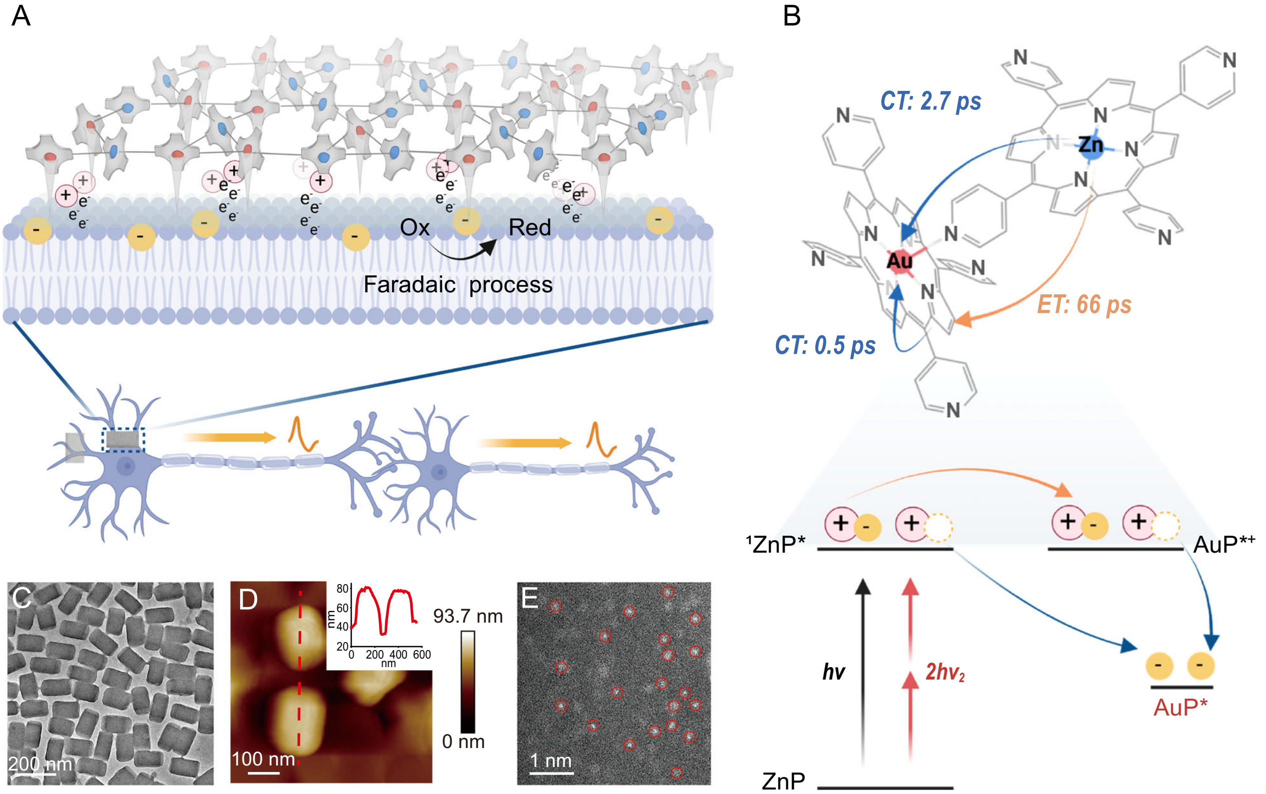

Fig. 1 | The photoelectron transfer and charge injection process of ZnAuPN for neuromodulation. A The design of a bimetallic zinc and gold porphyrins self-assembled nanoelectrode array brings an optimal photoelectrical performance with high-efficient photoelectron transfer and charge injection in neurons. The 2D ZnAuPN prefers to tightly adhere to the outer membrane of neurons, and upon laser illumination, the excited electron will ultrafast transfer over porphyrin rings to accumulate near the undercoordinated Au-atom centers which serve as stimulating electrodes, forming the electron-rich Au points to allow for the robust charge injection at ZnAuPN/neuron interface. The Au atom as the reactive center causes the photoelectrochemical redox from oxidation (Ox) to reduction (Red) solution for Faradaic current injection in solution (Faradaic process). **B** ZnAuPN with enhanced nonlinear optical sensitivity can be excited by both visible one-photon and near-infrared two-photon. The ultrafast photoelectron transfer process is shown including both the intermolecular charge transfer (CT) (~2.7 ps) and energy transfer (ET) (~66 ps) from ZnP to the adjacent AuP^+, and the intramolecular CT (~0.5 ps) in single AuP^+, with the total transfer efficiency up to 97%. All these effects afford the high-efficient current injection for optical control on a single neuron at ms temporal resolution. **C** TEM image of ZnAuPN. **D** AFM image of ZnAuPN with the height profile in the insert figure. **E** HAADF-STEM image of ZnAuPN. Single Au atoms are indicated by red circles. Data are representative of at least three independent experiments with similar results.

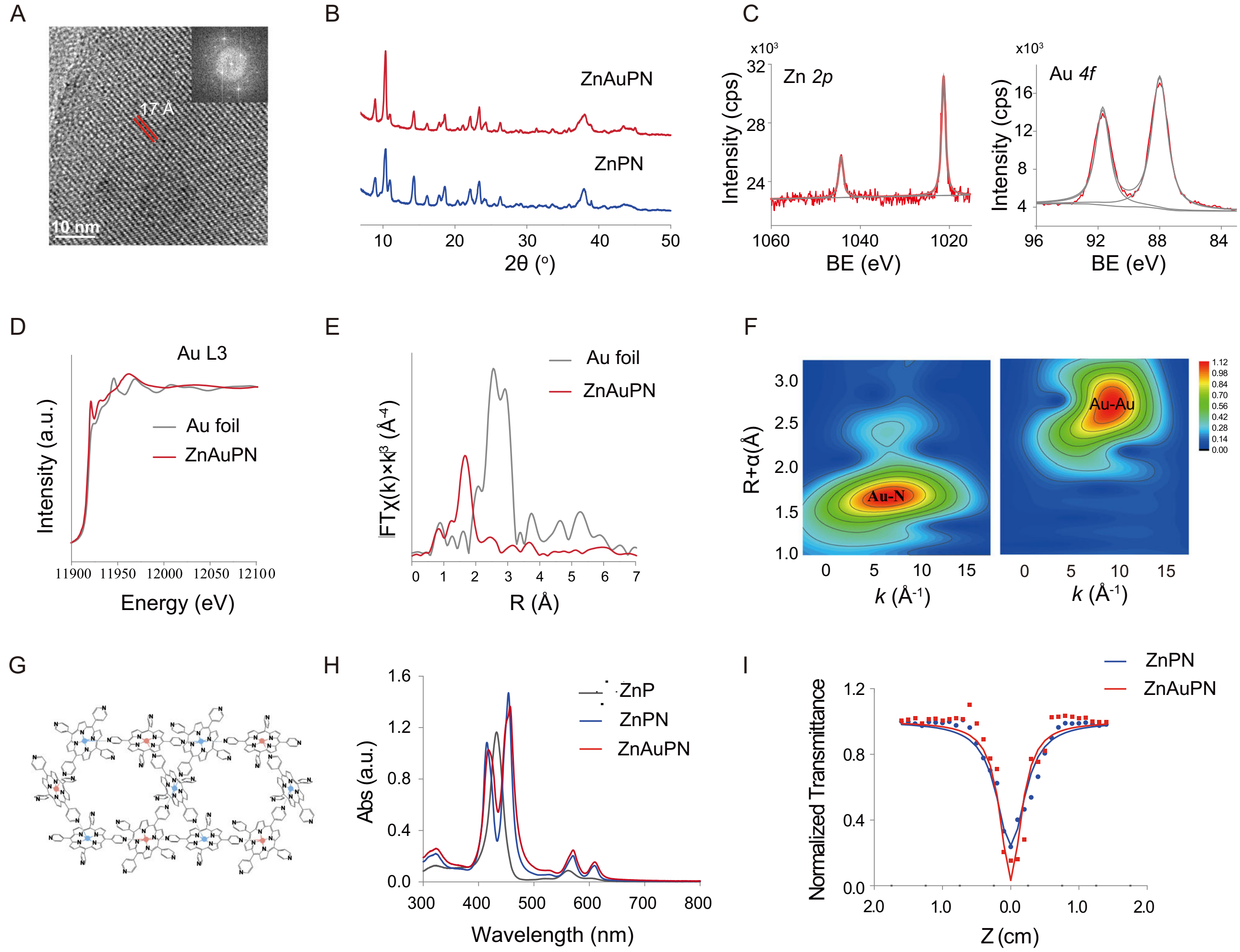

Fig. 2 | Materials synthesis and characterization. A HRTEM and FFT images of the ZnAuPN. **B** XRD of ZnPN and ZnAuPN. **C** XPS fine spectra of the Zn 2p and Au 4f of ZnAuPN. **D.** XANES spectra of the Au K-edge. **E** Fourier transforms (FT) k^3-weighted $\chi(k)$-a function of the EXAFS spectra for Au K-edge. **F** Wavelet transform of ZnAuPN and Au foil samples. **G** The supramolecular connectivity scheme in the 3D coordination of ZnP and AuP. **H** The UV–Visible absorption spectra of monomeric ZnP, ZnPN, and ZnAuPN samples. **I** The open-aperture Z-scan signature of ZnPN and ZnAuPN at 800 nm fs laser.

atomic force microscope (AFM). The single bright spots, under the aberration-corrected high-angle annular dark-field scanning transmission electron microscopy (HAADF-STEM) analysis, suggest Au as single atom embedded in ZnAuPN (Fig. 1E)[22].

The HRTEM and FFT illustration images showed the good crystallinity of the ZnAuPN and the lattice spacing was 17 Å (Fig. 2A). X-ray diffraction (XRD) patterns proved that ZnAuPN was isostructural to monometallic self-assembled ZnPN analogs (Fig. 2B). X-ray photoelectron spectroscopy (XPS) was used to investigate the valence states of metal in ZnAuPN (Fig. 2C), which exhibited a single Zn($2p_{3/2}$) peak at 1022.4 eV, corresponding to Zn^{2+}, and two peaks at 91.7 eV (Au $4f_{5/2}$) and 88.0 eV (Au $4f_{7/2}$), corresponding to Au^{3+}, which was in good accordance with the X-ray absorption near edge structure (XANES) results[23]. To further confirm the single-Au-atom structure, X-ray absorption fine structure (XAFS) spectroscopy was conducted. The Au L3-edge in XANES curve of ZnAuPN suggested the oxidation state of the Au^{3+} atom (Fig. 2D). According to the powerful resolution in both *k* and *R* spaces of wavelet transform, the first shell in the sample was mainly Au-N coordination for ZnAuPN (Fig. 2E, F and Fig. S2) but Au-Au for Au foil as a reference, demonstrating that Au atoms were atomically dispersed in ZnAuPN. Based on the above fitting, Au was found atomically anchored in the center of porphyrin structures and coordinated with nitrogen atoms in both porphyrin ring and adjacent molecules, which possessed the same coordination environment with the topology of the coordination pattern shown in Fig. 2G. In comparison to monomeric ZnP, the absorption spectra of ZnPN and ZnAuPN all showed the obvious red-shift in visible region, due to the expected Soret and Q-band transitions (Fig. 2H)[24]. Using the Z-scan technique, the nonlinear optical properties were measured[25]. The light transmittance showed an obvious left-right symmetric valley shape, with the two-photon absorption cross section of ZnAuPN increased from 2385 GM of ZnPN to 4369 GM (Fig. 2I) owing to the contribution of Au atom. Since NIR light can penetrate deep through tissues, the enhanced nonlinear property suggests ZnAuPN is favorable for high-spatial-resolution modulation of neurons and fluorescence tracing.

The photoinduced energy and charge transfer properties of ZnAuPN

The steady-state fluorescence spectra of ZnAuPN showed that the intrinsic fluorescence of ZnP was quenched compared to the ZnPN reference (Fig. 3A, B), which suggested the decrease in the lifetime of the singlet excited ZnP* in ZnAuPN since AuP^+ is nonfluorescent[14]. The reduced fluorescence lifetime of ZnAuPN can be used to predict the spontaneity of energy and electron transfer processes that occurred from ZnP to AuP^+. Time-correlated single photon counting (TCSPC) kinetics (shown in Fig. 3C) exhibited an ultra-short lifetime of ~66 ps in ZnAuPN (this signal is not detected in ZnPN) with the calculated rate of about $1.485 \times 10^{10}\ s^{-1}$ and the calculated fluorescence quenching

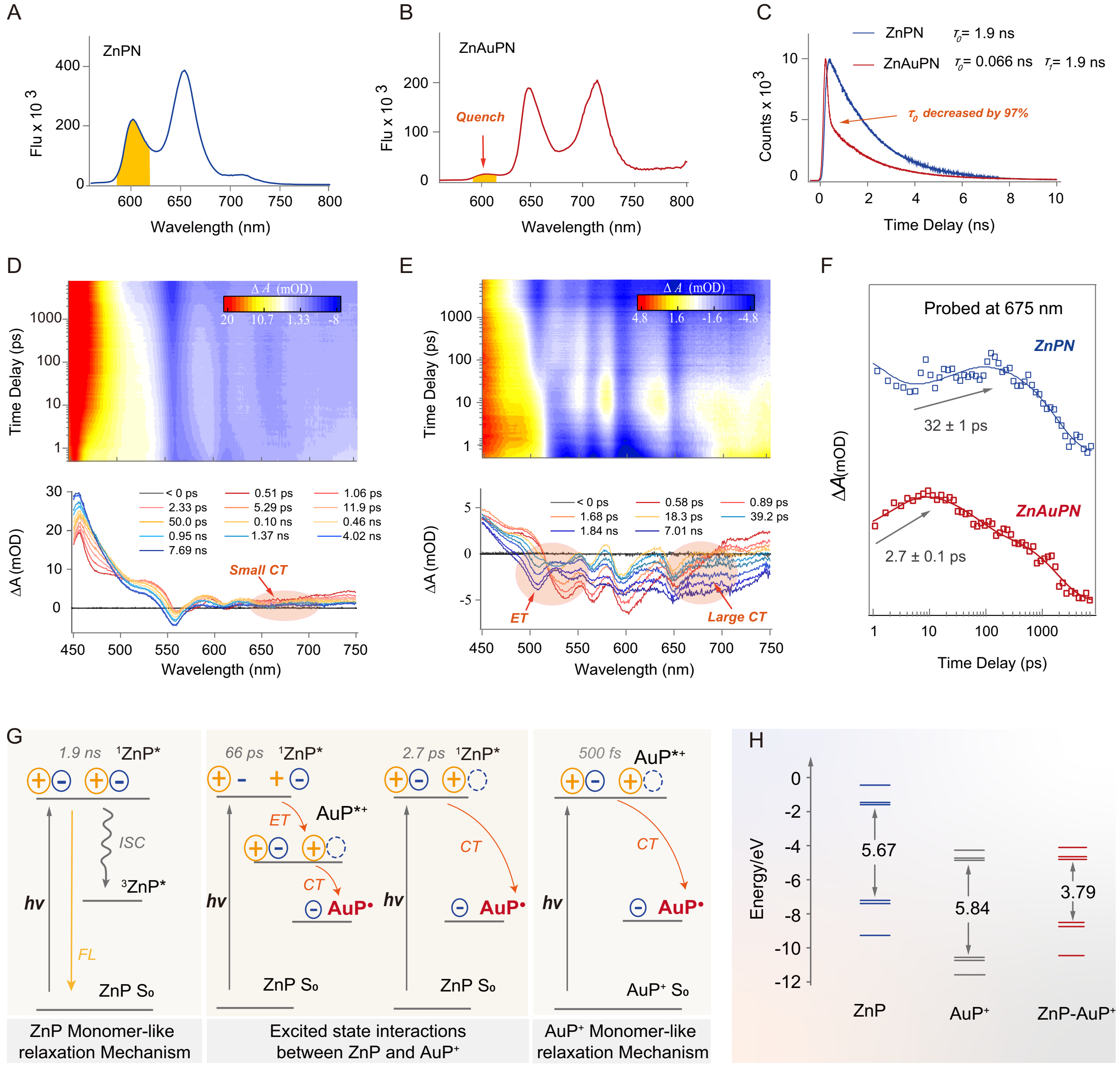

Fig. 3 | Photoinduced energy and charge transfer in ZnAuPN. The steady-state emission spectra of ZnPN (**A**) and ZnAuPN (**B**). **C** The time-correlated single photon counting kinetics of ZnPN and ZnAuPN were examined, with excitation at 420 nm and emission at 603 nm. Femtosecond time-resolved broadband transient absorption spectra of ZnPN (**D**) and ZnAuPN (**E**). **F** The TA kinetic trace of ZnPN and ZnAuPN probed at 675 nm. **G** The proposed excited relaxation mechanism of ZnAuPN. **H** The frontier orbital analysis results of monomeric ZnP, AuP^+, and ZnP-AuP^+ dimer. Data are representative of at least three independent experiments with similar results.

efficiency about 97%, indicating that the energy or charge transfer between ZnP and AuP^+ was very efficient. Data were representative of at least three independent experiments with similar results.

Femtosecond time-resolved broadband transient absorption (TA) spectra was further carried out on ZnPN and ZnAuPN samples dissolved in ethanol under the 420 nm laser excitation. For ZnPN, Fig. 3D showed the ultrafast generation of typical spectra of ZnP S_1 state with excited state absorption band (ESA) peaked at 465 nm and shouldered around 520 nm[26,27]. The transient spectra after 1000 ps still showed the characteristics of the ZnP S_1 state. Meanwhile, a slight positive band can be observed in the 650-700 nm region after ca. 200 ps, which was consistent with the typical absorption of oxidized $ZnP^{•+}$, suggesting a small part of the excited state population decay to the charge transfer state[15]. The electron difference map of ZnP units in the S_1 state can contribute the CT between ZnP units[15,28]. Moreover, the generation of the spectra ranging from 400–450 nm was assigned to the intersystem crossing (ISC) to triplet state[15,28,29]. Global fitting the TA data yields lifetimes of 1.5 ± 0.1 ps (τ_1), 32 ± 1 ps (τ_2), and 1.8 ± 0.2 ns (τ_3). τ_1 was related to the relaxation from S_n to S_1, while τ_3 was consistent with the fluorescence lifetime extracted from TCSPC and should be assigned to the decay of S_1[15]. The 1.5 ps and 1.8 ns components observed in ZnPN align well with those reported for the ZnP molecule in solution. However, due to the significantly larger size of ZnPN, fast vibrational relaxation with lifetimes in the tens of picoseconds is not expected. Instead, the build-up lifetime corresponding to the typical spectrum of $ZnP^{•+}$ is 32 ± 1.0 ps in ZnPN (Fig. 3F), indicating that charge separation is responsible for τ_2[30]. In contrast, for ZnAuPN, Fig. 3E showed significant differences in the spectral shape and lifetimes, as an ESA band with one absorption maximum blow 450 nm and shoulder peak at 480 nm, and several bleach bands ranging between 500 nm and 700 nm can be probed concurrently right after the excitation pulse. In the next ~10 ps, the typical absorption band of $ZnP•^+$ (650–700 nm) builds up sharply. Furthermore, bleaching of the Q (1, 0) band of ZnP centered around 540 nm recovers in lock with the generation of the bleaching band of AuP^+ centered at 500 nm within ca. 300 ps timely, suggesting the occurrence of energy transfer between ZnP and AuP^+. The TA data can be best fitted with a four-exponential decay function, yielding the lifetimes of 500 ± 100 fs (τ_1, AuP•), 2.7 ± 0.1 ps (τ_2, AuP•), 66 ± 1 ps (τ_3, AuP^{*+}) and 1.9 ± 0.2 ns (τ_4, $^3ZnP^*$). In the realm of the ZnAuPN nanosystem, considering the likelihood of intricate interactions between the ZnP and AuP^+ substructures, photoexcitation at a wavelength of 420 nm was anticipated to elicit concurrent relaxation mechanisms analogous to those exhibited by the discrete ZnP and AuP^+ units, alongside intermolecular processes encompassing excited-staete energy transfer and charge transfer between ZnP and AuP^+. The proposed excited state relaxation mechanism was shown in Fig. 3G. Similar to ZnPN, τ_4 is assigned to the decay of S_1 of ZnP. Since τ_2 also correlates with the build-up of $ZnP^{•+}$, it was assigned to the charge transfer between ZnP and AuP^+. As shown in Fig. 3F, the build-up process of $ZnP^{•+}$ in ZnAuPN occurs an order of magnitude faster than in ZnPN, suggesting that charge separation between ZnP and AuP^+ was more efficient, effectively quenching the intramolecular charge separation of ZnP (32 ± 1.0 ps) observed in ZnPN. Moreover, we propose that τ_1 is attributed to intramolecular charge transfer in AuP^+, while the newly emerging τ_3 is related to energy transfer between ZnP and AuP^+, consistent with the results from the TCSPC experiments. It is worth noting that the effective excited state charge transfer present in ZnAuPN can proficiently suppress ISC process, thereby mitigating potential adverse effects arising from the triplet state[14]. Lastly, the S_2 to S_1 internal conversion of ZnP (1.5 ps) was also expected to occur in ZnAuPN; however, this signal was obscured by the stronger TA signal of charge separation between ZnP and AuP^+, due to its relatively weak intensity and similar lifetime.

The above analysis leads to the proposed excitation relaxation mechanism of ZnAuPN, as illustrated in Fig. 3G. Clearly, compared with ZnPN, not only has charge transfer characteristics been significantly enhanced but also there was a new energy transfer channel involved in ZnAuPN. To further elucidate the dynamics and mechanisms of the photoinduced charge transfer and recombination process, the biporphyrins system was theoretically simulated via the metal-ligand axial coordination linking (Fig. 3H). As illuminated by the frontier orbital analysis, the highest occupied molecular orbital (HOMO) was mostly localized on zinc porphyrin with energy levels in the range of −10.5 to −8.55 eV, and the lowest unoccupied molecular orbital (LUMO) was on gold porphyrin with the energy levels in the range of −4.76 to −4.12 eV, which reveals the significantly reduced HOMO–LUMO gap in comparison to ZnP or AuP^+ alone. Upon the light excitation, it results in the formation of singlet excitation station ZnP*, which can undergo a fast relaxation to the ground state as well as charge/energy transfer to the adjacent gold porphyrin. This facilitates the electron flow into the single Au-site and ultimately leads to the significant energy transfer effect that quenches the intrinsic fluorescence of ZnP, as being observed above.

The current injection properties of ZnAuPN

The photocurrent output from ZnAuPN in physiological solution was measured by using a patch-clamp setup[3,31]. The measurements were performed in a voltage-clamp mode with laser irradiation on the quartz patch pipettes (Fig. S3a). As shown in Fig. S3b–e, the photocurrents increased obviously with the increase of laser power density and irradiation time. The frequency of the photocurrent output trains in response to the applied optical stimulation (Fig. S3f) indicates the highly stable photoelectrical properties. Notably, the photocurrents had a great relationship with the Zn/Au ratio in ZnAuPN. Compared with that from ZnPN without Au, about 20 times enhancement of current density was achieved when the Zn/Au ratio reaches ~0.3:1 in XPS and ~1:1 in EDS, yielding a massive photocurrent with the current output up to ~10.0 nA (Fig. 4A), which was much higher than the current of ~0.12 nA of silicon nanowire electrode[3]. Further increase of Au component proportion in ZnAuPN resulted in the current intensity gradually decreasing owing to the concentration quenching effect (Fig. S3g, h).

The charge injection dynamics of ZnAuPN materials was studied in methylene blue solution under oxygen-free condition since methylene blue can undergo electron reduction reaction with an accompanying color change from blue to colorless[32]. As shown in Fig. 4B, the color changing of methylene blue with ZnAuPN proceeded about 1.5-time faster than that with ZnPN under the same light treatment, as the undercoordinated Au atom active sites in ZnAuPN favor the charge injection in solution.

It was worth noting that the slope of photocurrent increase after the pulsed laser irradiation became faster with the amount of Au increased in ZnAuPN at the same time point, independent of the excitation light intensity (Fig. 4C and Fig. S3i). This larger slope originated from the shorter cutoff length of exciton migration by the heterojunction co-built by the p-type AuP^+ and n-type ZnP as well as the high-efficient charge injection in solution via the single Au atom centers. This is important for improving the temporal precision of photo signals inputs and nerve computations and outputs. For porphyrins alone, they have a wide spectral absorption range and a designable structure and function and have been used to photoinduce H_2O_2 production[33,34]. After being assembled into semiconductors, ROS can be formed by further redox reaction after photogenerated carrier separation, including O_2 reduction reaction and water oxidation reaction processe[35]. To evaluate the generation of H_2O_2 in a controlled manner, we established four experimental groups: Control, Laser, ZnAuNP, and ZnAuNP + Laser. Following the experimental protocol outlined in the Tian group's paper[36,37], we measured the samples after illumination for 0, 5, 10 min. Compared with other groups, ZnAuNP produced H_2O_2 under photoirradiation, and the H_2O_2 generation was related to the illumination time, indicating that ZnAuNP exhibited controllable production of H_2O_2 upon illumination (Fig. S4). This result aligns with our expectations, as ZnAuNP facilitates exciton separation and electron migration, leading to the formation of a long-lived charge-separated state that contributes to the production of peroxide.

Neuromodulation by ZnAuPN in primary rat cortical neurons

ZnAuPN was first used for photo-control neuronal activities in vitro, monitored by imaging the influx of calcium ions[25,38]. Rat cortical neurons in primary culture, showing positive expression of neuronal nuclei (NeuN), a typical neuronal marker, were cultured for 15 days in vitro (Fig. 4D). The ZnAuPN adhered to the outer membranes of neurons as well as the synapsis due to their 2D structure and negative surface potential, as proved by the uniform distribution of red fluorescence (ZnAuPN: 561 nm laser excitation, 600 nm fluorescence emission) (Fig. 4E) and SEM image (Fig. 4F). Under a laser scanning confocal microscope, using the fluorescence Ca^{2+} indicator Cal-520 AM (AAT Bioquest), the intracellular Ca^{2+} signal (green fluorescence: 488 nm laser excitation, 514 nm fluorescence emission) increased immediately upon 561 nm laser illumination on neurons and returned to the resting level after turning off the 561 nm laser. By contrast, laser irradiation or ZnAuPN alone had no significant effect on neuronal activities (Fig. 4G). Notably, 800 nm fs laser stimulation also induced the stimulated rises of Ca^{2+} in ZnAuPN pre-cultured neurons (Fig. 4H), suggesting the potential of ZnAuPN as a near-infrared optoelectrode for far-field photomodulation of neurons. The whole-cell current-clamp setup was further used to record the neural firing upon 670 nm laser illumination. An excitability curve was simulated using a

https://doi.org/10.1038/s41467-024-54325-8

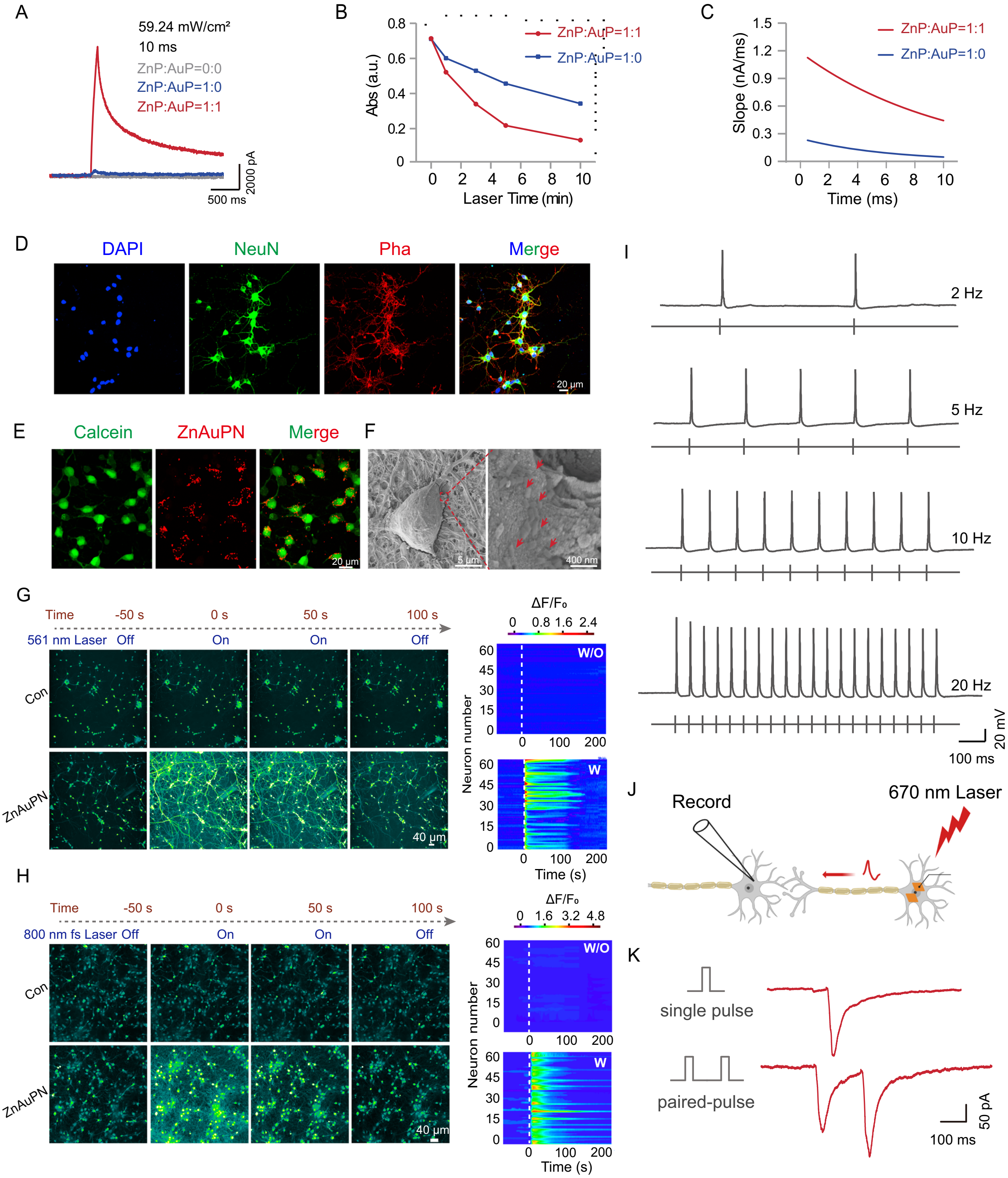

Fig. 4 | Photocurent measurement and neuromodulation by ZnAuPN in primary rat cortical neurons. A Photocurrent traces of ZnAuPN with different ratios of ZnP/AuP$^+$ under 670 nm laser of 59.24 mW/cm^2 for 10 ms duration irradiation. **B** The color-changing dynamics of methylene blue in ZnAuPN (ZnP/AuP$^+$ ~ 1:1) and ZnPN (ZnP/AuP$^+$ ~ 1:0) under 670 nm laser of 59.24 mW/cm^2 for 1 min duration irradiation. **C** The rising slope of photocurrent from ZnAuPN with different ratios of ZnP and AuP. **D** NeuN immunostaining in rat cortical neurons. DAPI staining the inner core of neurons. Pha (Phalloidin) markered the actin. Fluorescence image (**E**) and SEM images (**F**) of ZnAuPN adhering to the outer membrane of neurons. **G** Calcium imaging of neurons without (Con) or with ZnAuPN (ZnAuPN). 561 nm laser was used as a stimulation laser to induce the photocurrent output of ZnAuPN. 488 nm laser was used to excite the Ca^{2+} indicator Cal-520 AM for calcium imaging. **H** Calcium imaging of neurons without (Con) or with ZnAuPN (ZnAuPN). 800 nm fs laser (10^5 ~ 10^6 W/cm^2) was used as a stimulation laser to induce the photocurrent output of ZnAuPN. 488 nm laser was used to excite the Ca^{2+} indicator Cal-520 AM for calcium imaging. **I** Representative action potential traces recording of a neuron exposed to 670 nm pulse laser at different frequencies. **J** The scheme of the evoke postsynaptic currents tests recording on a postsynaptic neuron by illuminating ZnAuPN nanosheets attached to a presynaptic neuron with a single-pulse or paired-pulse laser. Postsynaptic neurons were patch clamped in the voltage-clamp whole-cell mode. **K** Representative traces of the evoked postsynaptic currents. Data are representative of at least three independent experiments with similar results.

hyperbolic function to determine the laser power required for action potential generation (Fig. S5). Our results indicate that an energy density of ~17.5 μJ/cm² is sufficient to initiate an action potential. As shown in Fig. 4I, neurons were able to generate trains of action potentials with frequencies responsive to the applied optical stimulation, suggesting the precise modulation of single-neuron activity. Moreover, the negligible reduction of peak potential suggests a negligible effect on cell activity during light stimulation on the timescales explored here.

Neuromodulation of neural circuits by ZnAuPN

ZnAuPN was further used to modulate neural circuits as the functional units of the nervous system, as controlling neural circuits is important for sensory information processing, homeostasis maintenance, behaviors driving, learning, and memory[38]. The primary neurons were cultured for up to 12 days to ensure neural network formation. With the postsynaptic neuron being concurrently recorded in voltage-clamp setup (Fig. 4J), we found that ZnAuPN irradiated by 670 nm laser could evoke a large excitatory postsynaptic current (eEPSC) at an average laser power density of 59.24 mW/cm² and 10 ms pulse duration. To further evaluate the presynaptic function, we recorded the paired-pulse response at a laser interpulse-interval of 100 ms and observed the paired-pulse facilitation (PPF) as a form of short-term synaptic plasticity[39] (Fig. 4K). By contrast, laser or ZnAuPN alone could not induce a response in neurons. Notably, our findings indicate that prolonged co-incubation of ZnAuPN with cells does not result in significant cytotoxicity (Fig. S6). Additionally, the presence of ZnAuPN, with or without laser irradiation, had no significant effect on cell viability, as confirmed by the MTT assay (Fig. S7). These results suggested that ZnAuPN can be a promising nano-optoelectrode for the study of neural network functions without gene transfection and gene expression processes.

Far-field optical modulation on neurons in mouse motor cortex

To test the effectiveness of ZnAuPN in vivo, the multi-channel electrophysiological recording system was used to measure the real-time neuronal activity in the specific region and pathway. 1.5 μL ZnAuPN at a concentration of 50 μg/mL was stereotactically pre-injected into the mouse secondary motor cortex (M2), with the multi-channel electrodes implanted at the same region. In vivo electrophysiological recording was performed in awake mice two days later. Without the use of optical fiber, the 670 nm laser was mounted outside the skull of the mouse as a stimulus light source (Fig. 5A). Our recorded signals were sorted as the spontaneous and stimulated spike-like events, which all showed typical extracellular electrophysiological recording. The representative electrophysiological signals and the corresponding quantified raster plots from the raw data were displayed in Fig. 5B. Upon 670 nm laser irradiation on a mouse with ZnAuPN, the motor cortex was activated with significantly enhanced spike firing rate up to ~45 Hz, in comparison to the intrinsic spontaneous firing rate of ~10 Hz (Fig. 5C–E). ZnAuPN or laser alone had no obvious effect on neuronal activity (Fig. 5F and Fig. S8). Notably, ZnAuPN remained effective after being injected into brain tissue for 28 days (Fig. S9a, b). Moreover, the morphology and crystal structure of ZnAuNP did not change significantly before and after long-term illumination (Fig. S10a, b). While the ZnPN had no obvious effect on neuronal activity (Fig. S11a, b). Meanwhile, we observed spontaneous movements in mice and found that irradiation of the motor cortex with ZnAuPN significantly increased these movements (Fig. 5G, H). In contrast, irradiation of the motor cortex with ZnPN did not produce a significant change in spontaneous activity (Fig. S11c, d). Furthermore, when performing two-photon extraction irradiation at 800 nm, we observed the generation of electromyography (EMG) signals in the hindlimbs of mice previously injected with ZnAuPN in the M2 (+Laser, +ZnAuPN). In contrast, control mice injected with ZnAuPN or laser alone did not exhibit detectable EMG signals (Fig. 5I). This discovery underscores the promising potential of deep brain modulation. Together with molecular levels of c-fos expression significantly increased in motor cortex neurons with ZnAuPN after 670 nm laser illumination 2 h later, while no such increase was seen in the ZnPN group, indicating that light-modulated ZnAuPN effectively facilitates local modulation of neuronal activity (Fig. 5J, L and Fig. S11e–g). Furthermore, the mouse brain tissues were collected 30 days later after ZnAuPN or ZnPN treatment, Glial fibrillary acidic proteins (GFAPs) expressed in the central nervous system in astrocyte cells were stained to reflect the inflammatory state of the brain, and as shown in Fig. 5K–M and Fig. S11f–h, the numbers of GFAP+ cells have no significant difference when compared with that in controls, indicating excellent biocompatibility of ZnAuPN for the safe use in organisms.

Discussion

In summary, we constructed bimetallic zinc(II) and gold(III) porphyrins as nanoscale photoelectrodes for precise modulation of neuronal activities with high spatiotemporal precision. This innovative bisporphyrin Bionics design enhances light harvesting and intramolecular electron transfer, facilitating the efficient flow of photoelectrons from ZnP to AuP$^+$. The incorporation of single gold atom centers serves as a stimulation electrode array, effectively injecting current into neurons via Faradaic processes[9,40]. Compared with other photoelectrode neural stimulation nanomaterials, our photoelectrodes had some particular features, including high charge per pulse energy, low energy per pulse for action potential initiation, a wide range of excitation light wavelength from visible to NIR for both in vitro and in vivo neuromodulation, and low power density for high biosafety (Supplementary dataset 1). This method offers a simple alternative to optogenetics, eliminating the need for gene transfection[41,42]. Moreover, the required laser intensity decreases by approximately five times compared to the laser intensity of 300–400 mW/cm² used in optogenetics, thereby preventing potential thermal damage to tissues. These nanoscale photoelectrodes not only enable the precise modulation of single neurons and even complex neural circuits for neurobiological research, but they also provide a wide range of applications in the non-invasive treatment of neurological diseases, such as drug addiction, diabetic peripheral neuropathy, and vision restoration.

Methods

Materials and reagents

Zinc 5,10,15,20-tetrapyridylporphyrin (ZnTPyP) was purchased from J&K Scientific LTD. **Sodium hydroxide** (NaOH), **sodium dodecyl sulfate** (SDS), **hydrochloric acid** (HCl, 36% ~ 38%), **ethanol, N, N-Dimethylformamide** (DMF) and ethanol were purchased from Sinopharm Chemical Reagent Co., Ltd. (Beijing, China). **Poly-D-lysine** (PDL), **chloroauric acid hydrate** ($HAuCl_4 \cdot xH_2O$) were obtained from sigma-Aldrich. All reagents were of analytical grade and were used without further purification.

Animals. C57BL/6 J male mice (8–10 weeks) and 16-day Shjh:SD pregnant rats were purchased from Shanghai Jihui Laboratory Animal Care Co. All animals were housed separately under specific pathogen-free (SPF) conditions at East China Normal University (10 h:14 h light/dark cycle, temperature 20–26 °C, humidity 40–70%). The study protocols were approved by the Animal Care and Use Committee of East China Normal University, with the Animal Experimental Ethical Inspection number: m$^+$R20190701. All surgeries were performed under general anesthesia to minimize suffering. Mice in the experimental groups were randomly assigned.

Materials characterization

Images of the materials were obtained by transmission electron microscopy (TEM, FEI Tecnai G2 F30) and scanning electron

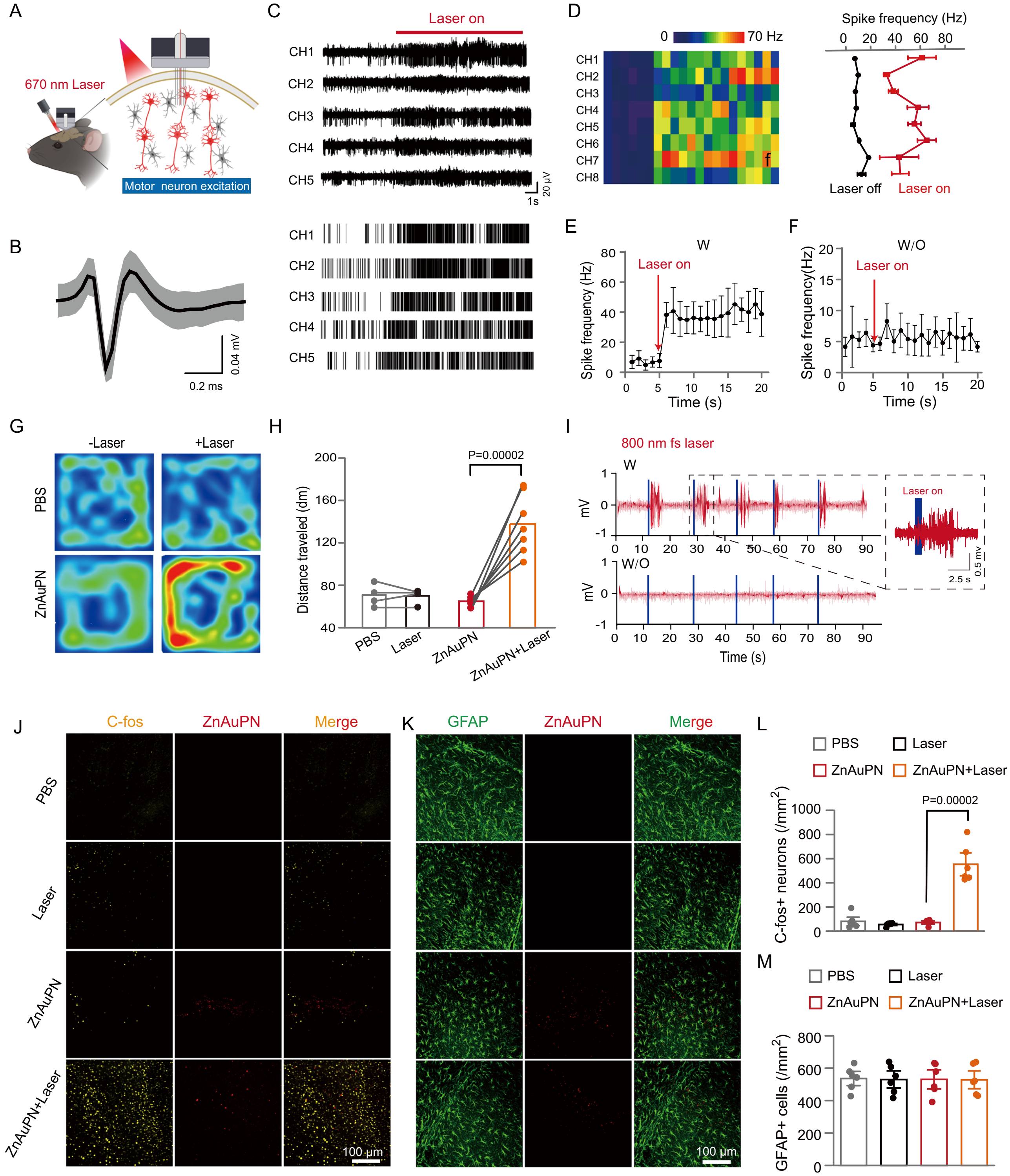

microscopy (SEM, Zeiss Ultra 55). The UV/Vis absorption spectrum was obtained using the UV–Vis Spectrophotometer (Shimadzu UV-3600 Plus spectrophotometer). The concentrations of Zn/Au ions were obtained by inductively coupled plasma optical emission spectroscopy (ICP-OES, ThermoFisher Icap 7400). The crystal structure of the materials was obtained by X-ray diffractometer patterns (XRD, Rigaku Ultima IV X-ray diffractometer with Cu K radiation). Atomic force microscopy (AFM) images were acquired on a Fast Scan atomic force microscope (Bruker) under Tapping mode. The X-ray photoelectron spectroscopy (XPS) measurements were performed on Shimadzu/Kratos AXIS SUPRA+. XANES and EXAFS data were carried out at Shanghai Synchrotron Radiation Facility (SSRF), China. The transmittance of materials through a finite aperture as a function of the sample position z was measured with respect to the focal plane on a special ultrafast laser testing system equipped with fs laser (ASTRELLA, 1000 Hz, 120 fs).

Synthesis of ZnPN and ZnAuPN

To synthesize ZnPN, SDS was dissolved in 5 mL deionized water (5 mM) and then 0.5 mL of ZnTPyP solution (0.01 M ZnTPyP dissolved in 0.2 M HCl) was quickly injected into the above solution. Finally, sodium hydroxide was added drop by drop to adjust the pH of the solution to

Fig. 5 | Extracranial 670 nm laser and 800 nm fs laser neuromodulation of the mouse motor cortex. A Illustration of the far-field photomodulation experiment in vivo. A multichannel recording electrode was implanted in the specific brain region with ZnAuPN pre-injection. 670 nm laser was applied as extracranial irradiation (Created in BioRender. Liu, Y. (2023) BioRender.com/t60d379). **B** A mean neuron-firing waveform from the spontaneous and stimulation-evoked events.The results are shown as mean ± SEM. **C** Example traces of the recorded raw signals (top) and the corresponding spike raster plots (bottom). **D** Heat maps of the channels from 1 to 8 (left) and the mean spontaneous and evoked mean neural response for the same channels in the heat map (right) during 15 s laser stimulation. The results are shown as mean ± SD by two-way ANOVA by Bonferroni's post hoc test, *n* = 4. Averaged spike frequency from the multichannel recording from mice with ZnAuPN (W) (**E**) or without ZnAuPN (W/O) (**F**). The results are shown as mean ± SD by two-way ANOVA by Bonferroni's post hoc test, *n* = 8. **G** The movement track of the mouse with or without ZnAuPN before and after 670 nm laser stimulation. **H** Statistical analysis of the movement distance of mice pre-injected with ZnAuPN or without ZnAuPN and with or without 670 nm laser irradiation. The results are shown as mean ± SEM by two-way ANOVA by Bonferroni's post hoc test, PBS and Laser group, *n* = 4; ZnAuPN and ZnAuPN + Laser group, *n* = 6. **I** EMG signals of the mouse with or without ZnAuPN before and after 800 nm fs laser stimulation. **J, K** Immunohistology of the C-fos expression in mice M2 that were collected 2 h later after different treatments (**J**) and the GFAP expressed in mice M2 that were collected 30 days later after different treatments (**K**). Statistical analysis for the number of C-fos$^+$ neurons (**L**) and the number of GFAP$^+$ neurons (**M**). The results are shown as mean ± SEM by two-way ANOVA by Bonferroni's post hoc test, *n* = 6 mice in each group. Data are representative of at least three independent experiments with similar results.

6.0 and stirred vigorously for 24 h. To synthesize ZnAuPN, different volumes of $HAuCl_4 \cdot xH_2O$ aqueous solution (2 mg Au per mL) were added to the ZnPN (1 mg/mL) dissolved in DMF and stirred at room temperature for 5 min. The mixture was then heated at 80 °C for 4 h. After the reaction, the sample was centrifugally washed with deionized water 3 times, and ZnAuPN was collected.

Ultrafast transient absorption (TA) spectroscopy

The TA data were collected using a femtosecond pump-probe spectrometer integrated with an ultrafast amplified laser system. The fundamental beam was produced by a Ti laser system (Astrella, 800 nm, 100 fs, 7 mJ/pulse, 1 kHz repetition rate, Coherent Inc.), which was split into two parts by a beam splitter. One portion was directed to an optical parametric amplifier (OPerA Solo, Coherent Inc.), which generated pulses at the required wavelength to serve as the pump beam. The remaining 800 nm beam was used for white-light generation, serving as the probe beam. The TA signals were measured with a femtosecond-to-microsecond TA spectrometer (Helios Fire, Ultrafast System). All samples were uniformly dispersed in ethanol, and during the measurements, the sample in the cell was continuously stirred under ambient conditions.

Two-photon properties

The two-photon absorption cross-section σ was calculated according to the following formula (1):

$$T(z) = 1 - \frac{\beta I_0 L}{2^{\frac{3}{2}}\left(1 + \left(\frac{z}{z0}\right)^2\right)} \tag{1}$$

$$\sigma = \frac{\beta h\upsilon \times 10^3}{Nc} \tag{2}$$

I_0: light intensity at the focus; L: the thickness of the sample; N: Avogadro constant; c: the concentration of solution; β: the nonlinear absorption coefficient.

In our experiment, the excitation light was 800 nm fs laser (1000 Hz, 120 fs), the lens focus length was 3 cm, the thickness of the sample was 1 mm, and the power used during the experiment was recorded.

Computational methods

All calculations were performed in the Gaussian 16 software. The wB97XD functional combined the basis set of def2-SVP was used for geometry optimization and frequency calculations. And 100 states were calculated for TDDFT calculations under the wB97XD/def2-SVP level. And all the exited state analysis was worried out by Multiwfn3.8(dev) package. ZnP, AuP$^+$, and ZnP-AuP$^+$, were used as models for the calculation.

XAFS data

The corresponding Au-foil was used as a reference to calibrate the energy and the XAFS data at the Au L3-edge of the ZnAuPN were recorded. The acquired EXAFS data reduction and analysis were processed in accordance with standard procedures using the Athena program.

Detection of electron injection of ZnPN and ZnAuPN in aqueous solution

The electron injection ability of different materials was verified by the methylene blue (MB) color change experiment under the condition of removing oxygen. Briefly, argon gas was continuously injected into MB for 30 min, and then 5 mg ZnPN or ZnAuPN was mixed with the above solution. Under the irradiation of red light (670 nm), the color of the mixed solution system changes. After centrifugation, the absorbance of MB solution at 664 nm was measured at different time points.

In vitro cytotoxicity assessment

Cells were seeded into a 96-well plate at a density of 10,000 cells per well and cultured at 37 °C for 24 h. Subsequently, different concentrations of ZnAuPN were added to the culture media and incubated for 24, 48, 72, and 96 h. After each incubation period, 100 μL of MTT solution (0.6 mg/mL in PBS) was added to each well and incubated for an additional 4 h. Absorbance was measured at 490 nm using a microplate reader following the addition of DMSO. Cell viability was expressed as a percentage relative to untreated control cells.

For light treatment, a 670 nm or 800 nm laser was used to irradiate the 96-well plate containing ZnAuPN at a concentration of 200 μg/mL for 1, 2, 3, 4, or 5 min. After irradiation, the cells were further incubated for 12 h, followed by the addition of 100 μL of MTT solution (0.6 mg/mL in PBS) and incubation for another 4 h. Absorbance was measured at 490 nm using a microplate reader after the addition of DMSO, and cell viability was calculated as a percentage relative to untreated control cells.

Primary culture of rat cortical neurons

On day 18 of pregnancy, the rats were anesthetized with halothane. Fetal brains were quickly removed and placed in ice-cold PBS. The tissues were then dissected and incubated in 0.05% trypsin-EDTA for 15 minutes at 37 °C, followed by gentle trituration using fire-polished pipettes. The cells were plated in poly-L-lysine-coated culture dishes, and neurons were cultured in Neurobasal medium supplemented with B27. The cultures were maintained at 37 °C in a humidified incubator with 5% CO_2. The medium was changed twice a week, and the cultures were used for assays 14–16 days after plating.

Confocal fluorescence imaging

ZnAuPN (150 μg/mL) was added to the rat primary neurons in culture dishes. After 12 h of co-incubation, the cells were washed three times with PBS. Luminescence imaging revealed that ZnAuPN nanoparticles were attached to the extracellular surface. For intracellular Ca^{2+} imaging, cortical neurons were co-incubated with Cal-520, AM (0.1 M, 4 µL, AAT Bioquest) for 2 h, followed by three PBS washes. Real-time changes in Ca^{2+} fluorescence intensity were observed using synchronous 561 nm laser or 800 nm femtosecond (fs) laser stimulation for 80 s, combined with visible laser imaging at 488 nm. The 561 nm laser from the confocal instrument (Nikon A1 + R-980) and the 800 nm fs laser (Leica TCS SP8) were used as continuous light sources in a standard confocal microscope.

Scanning electron microscopy

Rat primary neurons were cultured on glass coverslips. ZnAuPNs were added to the medium and incubated with the neurons for 12 h. The sample was then washed with PBS, followed by fixation with 2.5% glutaraldehyde and staining with 1% osmium tetroxide for 1 h at room temperature. Afterward, the sample was dehydrated using a graded ethanol series and dried at the critical point. Images were acquired using a Zeiss Ultra 55 field emission scanning electron microscope (FE-SEM).

Photocurrent measurements

One microliter ZnAuPN (2000 µg/mL) were deposited into quartz glass capillary tubes. Then the quartz capillary tube was pulled to produce pipettes with 2–4 MΩ resistances and filled with bath solution. These pipettes are then fitted to the patch-clamp device and current were recorded in voltage-clamp mode at 0 mV with 670 nm laser illumination. Laser pulse between 1 ms and 20 ms durations and 1–60 mW/cm^2 power were used.

Electrophysiology can be regarded as a precision electrochemical workstation used to detect changes in the electric potential and current across the cell membrane. The environment inside the micropipette simulates the intracellular environment, while the environment outside the micropipette simulates the extracellular environment. When ions in these internal and external environments are disturbed or exchanged, changes in membrane potential or membrane current occur, reflecting neuronal activity.

The PE effect of materials is usually studied using an electrochemical workstation, which relies on the effect of photogenerated charges on the distribution or movement of ions in electrolyte solutions. Typically, when photogenerated electrons and holes participate in redox reactions at the electrodes/electrolyte interface, photogenerated electrons reduce oxidants at the cathode, while photogenerated holes oxidize reductants at the anode. These redox reactions alter ionic charges concentrations, resulting in changes in the current measured by the electrode. These dynamic changes can be detected through the electrodes.

Similarly, when our samples are loaded into the micropipette chamber, the interaction between the photogenerated electrons alters the original charge distribution, which can be sensitively measured via the electrophysiology system. This test method has been used for qualitative comparison and analysis in other similar works[3].

Calculation of charge in a single neuron

The concentration of ZnAuPN in the culture dish containing neurons is 150 µg/mL. And when 1 µL of ZnAuPN (2000 µg/mL) is irradiated with a 670 nm laser for 10 ms, it can generate a charge of ~530 pC ($Q = IT$; Q: Quantity of charge; I: current; T: time). Therefore, based on calculations, the charge (Q) injected into single neurons is estimated to be around 4 pC within a 1 ms timeframe.

$$\text{Charge (Single neuron)} = \frac{\text{Total charge (530 pC)}}{2000/150} \tag{3}$$

In vitro neuron electrophysiology experiments

Brain neurons were patch-clamped in whole-cell current clamp configuration using an Axopatch 700B amplifier (Molecular Devices). Neurons were co-cultured with ZnAuPN (150 µg/mL) for 12 h to ensure effective attachment to the cells. After incubation, the cells were washed twice with a pre-configured bath solution (NaCl 132 mM, KCl 4 mM, $MgCl_2$ 1.2 mM, $CaCl_2$ 1.8 mM, HEPES 10 mM, glucose 5.5 mM, pH 7.4) to remove free particles, and then maintained in the same solution. Borosilicate glass pipettes, pulled on a CO_2 laser micropipette puller (Sutter Instruments P-2000), had resistances of 4 MΩ when filled with the internal pipette solution (K-Gluconic acid 110 mM, NaCl 10 mM, $MgCl_2$ 1 mM, EGTA 10 mM, HEPES 30 mM, Mg-ATP 3 mM, Na-GTP 0.3 mM, pH 7.2). Under current clamp configuration, spike firings were recorded with or without 670 nm laser irradiation. Evoked excitatory postsynaptic currents (EPSCs) were recorded in postsynaptic neurons upon stimulation of presynaptic neurons with ZnAuPN and 670 nm laser irradiation. PPF was elicited with paired laser stimuli at 100 ms intervals. Data acquisition was performed using pClamp10 (Molecular Devices, USA), with filtering applied during acquisition using a 2 kHz low-pass filter, and analysis was conducted offline with Clampfit 10.2 (Molecular Devices, USA).

In vivo electrophysiological recording

Nickel-titanium microwire electrodes (KD-MWA-F, KedouBC) were used for in vivo electrophysiological recordings following ZnAuPN injection in anesthetized mice. Four screws were implanted into the skull as grounding and reference electrodes. After the grounding screw was implanted, the electrodes were slowly inserted into the right motor cortex (anteroposterior (AP) +1.0 mm, mediolateral (ML) +0.5 mm, dorsoventral (DV) −0.5 mm). Once the target region was reached, the electrodes were secured to the skull with LELE® dental cement. The electrodes were connected to a high-throughput neural recording system (Zeus, Bio-Signal Technologies), with a 0–80 set screw serving as the reference. A 670 nm laser was illuminated at a power density of 24 mW/cm^2. Electrophysiological recordings were obtained at a sampling rate of 20 kHz with a 60 Hz notch filter. The recorded signals were analyzed using Offline Sorter x64 V4 and NeuroExplorer 5 x64.

Secondary motor cortex stimulation in vivo

Mice were anesthetized via intraperitoneal injection of urethane (Sigma, St. Louis, MO, USA; 2 g/kg) and secured in a stereotaxic apparatus (RWD Life Science, Shenzhen, China) for surgery. Anesthesia was confirmed using the toe pinch method before proceeding. To maintain body temperature, a homeothermic blanket set at 37 °C was placed beneath the anesthetized mice. Erythromycin was applied to both eyes throughout the experiment to prevent dryness. Hair from the mouse's head was removed using hair removal cream. A pre-injection of 1.5 µL ZnAuPN (50 µg/mL) was administered into the secondary motor cortex at stereotaxic coordinates: AP +1.0 mm, ML +0.5 mm, and DV −0.5 mm. The mice were then allowed to recover for 48 h before behavioral experiments commenced. Subsequently, the mice were placed in a 50 × 50 cm^2 open field and allowed to freely explore the area. A video camera recorded the mice for 2 min, with or without 670 nm laser stimulation.

In vivo electromyographic

To record EMG activity in hindlimb muscles while activating M2 neurons through 800 nm fs laser stimulation, we injected ZnAuPN (50 µg/mL) into the secondary motor cortex. After a two-day period, the mice were mildly anesthetized, and their hindlimbs were shaved. The electrode wires were exposed at their ends for approximately 1–2 mm, and then securely attached to the patch electrodes, which were subsequently affixed to the hindlimbs. Laser stimulation at 800 nm was delivered in trains of five trials, with each trial consisting of 5 s of stimulation followed by 10 s of rest. Throughout the laser stimulation, the EMG signals from the mouse's hindlimbs were recorded. The EMG signals were amplified and filtered using the Biotex Kyoto system from Japan, digitized with the Power 1401 device, and recorded using Spike2 Software at a sampling rate of 1000 Hz.

Histology study

Following the experiments, mice were deeply anesthetized with Pelltobarbitalum Natricum (40 mg/kg, i.p.) and perfused transcardially with 0.1 M PBS, followed by 4% paraformaldehyde in 0.1 M PBS. The brains were post-fixed in 4% paraformaldehyde overnight at 4 °C and then transferred to a 30% sucrose solution at 4 °C. Coronal brain sections, 20 or 30 μm thick, were cut using a cryostat and prepared for staining. Anti-c-fos antibody (Abcam, ab214672) and anti-GFAP antibody (Abcam, ab68428) were used for immunohistochemistry. GFAP staining was performed to assess the biocompatibility of ZnAuPN.

Statistical analysis

Statistical comparisons between two groups were performed using one-way analysis of variance (ANOVA) followed by Bonferroni post hoc analyses. For analyses involving multiple experimental groups, two-way repeated measures ANOVA or two-way ANOVA with Bonferroni post hoc analyses were used. Data are presented as individual values or expressed as mean ± SEM. Data are representative of at least three independent experiments with similar results. Data collection was conducted using Nikon A1 software 5.21.03, PatchClampFit 10.5, VisuTrack, and SlideViewer. Data plotting was performed with Jade 6.5, OriginPro 9.1, Clampfit 10.5, and GraphPad Prism 8.0.2.

Reporting summary

Further information on research design is available in the Nature Portfolio Reporting Summary linked to this article.

Data availability

The main data supporting the results in this study are available within the paper and its Supplementary Information. All data generated in this study are available from the corresponding authors. Source data are provided with this paper. The source data of linear graph and column diagram are provided as a Source Data file. Source data are provided with this paper.

References

1. Gradinaru, V. et al. Molecular and cellular approaches for diversifying and extending optogenetics. *Cell* **141**, 154–165 (2010).
2. Boyden, E. S., Zhang, F., Bamberg, E., Nagel, G. & Deisseroth, K. Millisecond-timescale, genetically targeted optical control of neural activity. *Nat. Neurosci.* **8**, 1263–1268 (2005).
3. Parameswaran, R. et al. Photoelectrochemical modulation of neuronal activity with free-standing coaxial silicon nanowires. *Nat. Nanotechnol.* **13**, 260 (2018).
4. Spagnolo, B. et al. Tapered fibertrodes for optoelectrical neural interfacing in small brain volumes with reduced artefacts. *Nat. Mater.* **21**, 826 (2022).
5. Stocking, K. C., Vazquez, A. L. & Kozai, T. D. Y. Intracortical neural stimulation with untethered, ultrasmall carbon fiber electrodes mediated by the photoelectric effect. *IEEE Trans. Biomed. Eng.* **66**, 2402–2412 (2019).
6. Pappas, T. C. et al. Nanoscale engineering of a cellular interface with semiconductor nanoparticle films for photoelectric stimulation of neurons. *Nano Lett.* **7**, 513–519 (2007).
7. Brown, M. A. et al. Determination of surface potential and electrical double-layer structure at the aqueous electrolyte-nanoparticle interface. *Phys Rev X* **6**, 011007 (2016).
8. Jiang, Y. W. & Tian, B. Z. Inorganic semiconductor biointerfaces. *Nat. Rev. Mater.* **3**, 473–490 (2018).
9. Jiang, Y. W. et al. Rational design of silicon structures for optically controlled multiscale biointerfaces. *Nat. Biomed. Eng.* **2**, 508–521 (2018).
10. O'Connell, C. D., Higgins, M. J., Moulton, S. E. & Wallace, G. G. Nano-bioelectronics dip-pen nanolithography. *J. Mater. Chem. C* **3**, 6431–6444 (2015).
11. Chen, J. et al. Non-Faradaic optoelectrodes for safe electrical neuromodulation. *Nat. Commun.* **15**, 405 (2024).
12. Wang, J. Y., Xue, P. Y., Jiang, Y. T., Huo, Y. & Zhan, X. W. The principles, design and applications of fused-ring electron acceptors. *Nat. Rev. Chem.* **6**, 614–634 (2022).
13. Ding, Y. B., Zhu, W. H. & Xie, Y. S. Development of ion chemosensors based on porphyrin analogues. *Chem. Rev.* **117**, 2203–2256 (2017).
14. Fukuzumi, S. et al. Metal-centered photoinduced electron transfer reduction of a gold(III) porphyrin cation linked with a zinc porphyrin to produce a long-lived charge-separated state in nonpolar solvents. *J. Am. Chem. Soc.* **125**, 14984–14985 (2003).
15. Andersson, M. et al. Long-range electron transfer in porphyrin-containing [2]-rotaxanes: tuning the rate by metal cation coordination. *J. Am. Chem. Soc.* **124**, 4347–4362 (2002).
16. Brun, A. M., Harriman, A., Heitz, V. & Sauvage, J. P. Charge-transfer across oblique bisporphyrins - 2-center photoactive molecules. *J. Am. Chem. Soc.* **113**, 8657–8663 (1991).
17. Kc, C. B. & D'Souza, F. Design and photochemical study of supramolecular donor-acceptor systems assembled via metal-ligand axial coordination. *Coord. Chem. Rev.* **322**, 104–141 (2016).
18. Nakanishi, S. T. & Whelan, P. J. Diversification of intrinsic motoneuron electrical properties during normal development and botulinum toxin-induced muscle paralysis in early postnatal mice. *J. Neurophysiol.* **103**, 2833–2845 (2010).
19. Göppert-Mayer, M. Über Elementarakte mit zwei quantensprüngen. *Ann. der Phys.* **401**, 273–294 (2006).
20. Wang, J. F. et al. Morphology-controlled synthesis and metalation of porphyrin nanoparticles with enhanced photocatalytic performance. *Nano Lett.* **16**, 6523–6528 (2016).
21. Yang, D. et al. Visible-light-switched electron transfer over single porphyrin-metal atom center for highly selective electroreduction of carbon dioxide. *Nat. Commun.* **10**, 3844 (2019).
22. He, T. et al. Zirconium-porphyrin-based metal-organic framework hollow nanotubes for immobilization of noble-metal single atoms. *Angew. Chem. Int. Ed.* **57**, 3493–3498 (2018).
23. Chen, Z. et al. Single-site Au catalyst for silane oxidation with water. *Adv. Mater.* **30**, 1704720 (2018).
24. Qiu, Y. F., Chen, P. L. & Liu, M. H. Evolution of various porphyrin nanostructures via an oil/aqueous medium: controlled self-assembly, further organization, and supramolecular chirality. *J. Am. Chem. Soc.* **132**, 9644–9652 (2010).
25. Nozawa, R. et al. Stacked antiaromatic porphyrins. *Nat. Commun.* **7**, 13620 (2016).
26. Brun, A. M., Harriman, A., Heitz, V. & Sauvage, J. P. Charge transfer across oblique bisporphyrins: two-center photoactive molecules. *J. Am. Chem. Soc.* **113**, 8657–8663 (1991).
27. Asahi, T. et al. Intramolecular photoinduced charge separation and charge recombination of the product ion pair states of a series of fixed-distance dyads of porphyrins and quinones: energy gap and temperature dependences of the rate constants. *J. Am. Chem. Soc.* **115**, 5665–5674 (1993).
28. Cho, S. et al. Structural factors determining photophysical properties of directly linked zinc(II) porphyrin dimers: linking position, dihedral angle, and linkage length. *J. Phys. Chem. B* **113**, 10619–10627 (2009).
29. Walters, V. A. et al. Electronic structure of triplet states of zinc(II) tetraphenylporphyrins. *J. Phys. Chem.* **99**, 1166–1171 (1995).

30. Abraham, B., Nieto-Pescador, J. & Gundlach, L. Ultrafast relaxation dynamics of photoexcited zinc-porphyrin: electronic-vibrational coupling. *J. Phys. Chem. Lett.* **7**, 3151–3156 (2016).
31. Park, J. et al. In situ electrochemical generation of nitric oxide for neuronal modulation. *Nat. Nanotechnol.* **15**, 690 (2020).
32. Chen, L. J. et al. Reductive-damage-induced intracellular maladaptation for cancer electronic interference therapy. *Chem* **8**, 866–879 (2022).
33. Jing, J. F., Li, J. S., Su, Y. G. & Zhu, Y. F. Non-covalently linked donor-acceptor interaction enhancing photocatalytic hydrogen evolution from porphyrin assembly. *Appl. Catal. B Environ.* **324**, 122284 (2023).
34. Zhang, Y. et al. H_2O_2 generation from O_2 and H_2O on a near-infrared absorbing porphyrin supramolecular photocatalyst. *Nat. Energy* **8**, 361–371 (2023).
35. Yong, Z. & Ma, T. Solar-to-H_2O_2 catalyzed by covalent organic frameworks. *Angew. Chem. Int. Ed.* **62**, e202308980 (2023).
36. Prominski, A. et al. Porosity-based heterojunctions enable leadless optoelectronic modulation of tissues. *Nat. Mater.* **21**, 647–655 (2022).
37. Phillips, A. W. et al. Gold-decorated silicon nanowire photocatalysts for intracellular production of hydrogen peroxide. *ACS Appl. Mater. Interfaces* **13**, 15490–15500 (2021).
38. Luo, L. Q. Architectures of neuronal circuits. *Science* **373**, 1103 (2021).
39. Jackman, S. L. & Regehr, W. G. The mechanisms and functions of synaptic facilitation. *Neuron* **94**, 447–464 (2017).
40. Derek, V., Rand, D., Migliaccio, L., Hanein, Y. & Głowacki, E. D. Untangling photofaradaic and photocapacitive effects in organic optoelectronic stimulation devices. *Front. Bioeng. Biotechnol.* **8**, 284 (2020).
41. Yizhar, O., Fenno, L. E., Davidson, T. J., Mogri, M. & Deisseroth, K. Optogenetics in neural systems. *Neuron* **71**, 9–34 (2011).
42. Banghart, M., Borges, K., Isacoff, E., Trauner, D. & Kramer, R. H. Light-activated ion channels for remote control of neuronal firing. *Nat. Neurosci.* **7**, 1381–1386 (2004).

Acknowledgements

The authors would greatly acknowledge the financial support by the Key Program of National Natural Science Foundation of China (No. 22235004, W.B.B), National Natural Science Foundation of China Youth Fund (Grant No. 52322213, Y.Y.L), Innovation Program of Shanghai Municipal Education Commission (No. 2023ZKZD01, W.B.B), the National Funds for General Projects (No. 52272269, Y.Y.L), National Science Foundation for the Young Scientists of China (No. 82202326, H.J.Z.), Natural Science Foundation of Shanghai (No. 21ZR1405300, Y.Y.L), Centre of Excellence programs (CE230100021, J.J.Z., and D.Y.J.). Thanks to Qingfeng Xiao in NIKON INSTRUMENTS (SHANGHAI) CO., LTD. for vigorous support in optical design and imaging.

Author contributions

W.B.B., Y.Y.L., D.Y.J., and J.C., conceived the idea and designed the study; Y.Y.L., F.X.C., H.J.Z. performed the material experiments and data analysis; X.L.W. and J.Q.C. performed the transient absorption spectra and data analysis; J.C., and F.X.C., L.W. cultured the in vitro neurons and performed cellular experiments; J.C. and M.N.G. performed the in vivo electrophysiological recording and data analysis; J.C. and F.X.C. performed the electrophysiological experiments both in vivo and in vitro; J.J.Z., D.Y.J., J.Z.X., L.Z., H.L., Y.H.S., M.Y.L., X.J.M., and X.W.J. contributed to discussion; W.B.B., Y.Y.L, and D.Y.J. supervised the research. All the authors participated in the preparation of the manuscript.

Competing interests

The authors declare no competing interests.

Additional information

Supplementary information The online version contains supplementary material available at https://doi.org/10.1038/s41467-024-54325-8.

Correspondence and requests for materials should be addressed to Jinquan Chen, Yanyan Liu, Dayong Jin or Wenbo Bu.

Peer review information *Nature Communications* thanks the anonymous reviewers for their contribution to the peer review of this work. A peer review file is available.

Reprints and permissions information is available at http://www.nature.com/reprints